Anisotropic giant magnetoresistance and Fermi surface topology in the layered compound $YbBi_2$

Xiaomeng Sun,[1,*] Fang Tang,[1,2,*] Xue Shen,[1] Wencong Sun,[3] Weiyao Zhao,[4] Yuyan Han,[5] Xucai Kan,[6] Shan Cong,[1] Lei Zhang,[1] Zhida Han,[1] Bin Qian,[1,†] Xuefan Jiang,[1] Shanshan Wang,[3,‡] Renkui Zheng,[7] and Yong Fang[1,§]

[1]*Jiangsu Laboratory of Advanced Functional Materials, School of Electronic and information Engineering, Changshu Institute of Technology, Changshu 215500, China*

[2]*Jiangsu Key Laboratory of Thin Films, School of Physical Science and Technology, Soochow University, Suzhou 215006, China*

[3]*School of Physics, Southeast University, Nanjing 211189, China*

[4]*ISEM, Innovation Campus, University of Wollongong, Wollongong, New South Wales 2500, Australia*

[5]*Anhui Province Key Laboratory of Condensed Matter Physics at Extreme Conditions, High Magnetic Field Laboratory, Hefei Institutes of Physical Science, Chinese Academy of Sciences, Hefei 230031, China*

[6]*Engineering Technology Research Center of Magnetic Materials, School of Physics & Materials Science, Anhui University, Hefei 230601, China*

[7]*School of Materials Science and Engineering, Nanchang University, Nanchang 330031, China*

(Received 27 October 2021; revised 24 April 2022; accepted 28 April 2022; published 10 May 2022)

Magnetoresistance in novel materials has been attracting ever-increasing attention since its mechanism is still the subject of intense debate and the physics behind these emergent phenomena remains a wild space to be explored. Here, we grow $YbBi_2$ single crystals and study their anisotropic giant magnetoresistance and Fermi surface topology via de Haas–van Alphen oscillation and Hall resistivity measurements, electronic band structure calculations, and so on. A detailed analysis of the angle-dependent quantum oscillations reveals the presence of nontrivial topological electronic states and several cylindrical Fermi surface sheets extended along the *b* axis. Hall resistivity data suggest that multiple charge carriers participate in the transport, and electron and hole densities are nearly balanced. These findings are further confirmed by theoretical calculations. After checking several possible mechanisms, the giant magnetoresistance ($\sim 1.2 \times 10^3$% at 14 T and 2 K) in $YbBi_2$ is ascribed to the carrier compensation instead of topological protection and open orbits. Additionally, we also find that Fermi surface anisotropy serves as a key element for the angular magnetoresistance in this compound. Our studies show that $YbBi_2$ can be not only a topologically nontrivial material, but also a prototype system to check familiar magnetoresistance mechanisms.

DOI: 10.1103/PhysRevB.105.195114

I. INTRODUCTION

Ever since nonsaturating magnetoresistance (MR) was discovered in WTe_2, there has been rapidly growing interest in studying this exotic physical phenomenon due to its complicated mechanisms and potential applications in electronic devices [1]. Shortly thereafter, such enthusiasm promptly spread to other systems, including Cd_3As_2 [2], *MPn* (*M* = Nb and Ta; *Pn* = P and As) [3,4], *RPn* (*R* = rare earth; *Pn* = Sb and Bi) [5–7], $PtBi_2$ [8], etc. Meanwhile, three prevalent mechanisms have been proposed for this MR [1,9–12]. One mechanism argues that in nontrivial electronic systems the lifting of topological protection by magnetic fields (*B*) could give rise to large MR [9]. Generally, in the Dirac semimetal Cd_3As_2 and Weyl semimetal *MPn* their MR can be understood by this way [2,9,13]. It is clear that this mechanism only works for the compounds with topological electronic states. Two other mechanisms assume that the nonsaturating MR is closely associated with the compensated Fermi surfaces (FSs) [1,5–7] and open FS [10,14–16], respectively. For the systems with compensated FSss (n_e–n_h), their MR shows B^2 dependences (MR $\sim \mu_e\mu_h B^2$) [1]. Here, n_e (n_h) and μ_e (μ_h) represent the electron (hole) density and mobility, respectively. It has been revealed that the MR in WTe_2 [1], $PtBi_2$ [8], *RPn* [17], $MoGe_2$ [18], etc., belongs to this category. For the systems with open FSs, their nonsaturating MR resulting from open orbits occurs only when the current (*I*) flows along the open orbits and *B* is applied in an orthogonal direction. As reported, the MR in ZrSiS [19], $MoAs_2$ [10], γ-$PtBi_2$ [14], SiP_2 [15],WP_2 [20], ReO_3 [21], $MoOCl_2$ [16], etc., is of this origin. It follows from the above that the actual mechanism responsible for nonsaturating MR differs by compounds.

$YbBi_2$ crystallizes in the $ZrSi_2$-type orthorhombic structure with a nonsymmorphic space group *Cmcm* [22]. Figure 1(a) displays its crystal structure with Yb and Bi atoms marked by the sky-blue and pink balls, respectively. As seen, two kinds of sheets, one consisting of Bi atoms and the other one composed of Yb and Bi atoms, are stacked along the *b* axis. This is reminiscent of the isostructural compounds $CaBi_2$ [23] and $YbSb_2$ [24] where the small and open FS sheets strongly affect their physical properties [25,26]. One may also find that

*These authors contributed equally to this work.
†njqb@cslg.edu.cn
‡wangss@seu.edu.cn
§fangyong@cslg.edu.cn

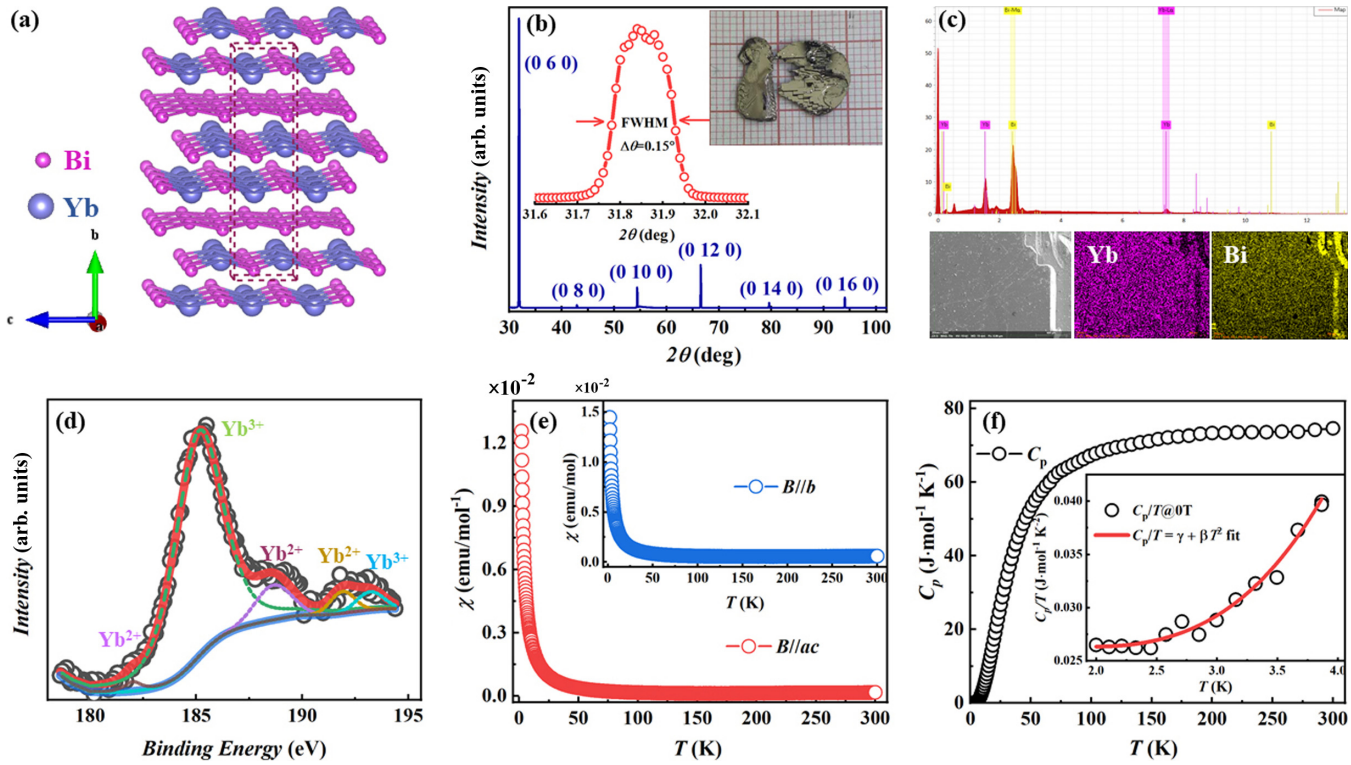

FIG. 1. (a) Schematic crystal structure of the layered $YbBi_2$. (b) XRD pattern of $YbBi_2$ single crystal, showing only the $(0k0)$ peaks. Insets plot the XRD pattern around (060) peak with a FWHM of approximately 0.15°, and single crystals used for this XRD scan on a millimeter scale. Panel (c) and its lower panel: EDX spectrum and elemental distributions for Yb and Bi, respectively. (d) Yb $4d$ core level spectra for $YbBi_2$. Panel (e) and its inset: χ as a function of T under 0.01 T for $B\|ac$ and $B\|b$, respectively. (f) T dependence of C_p of $YbBi_2$ at 0 T. Inset shows the low-T C_p and its fit with the equation $C_p/T = \gamma + \beta T^2$.

in the nonsymmorphic compounds, examples of which are $ZrTe_5$, ZrSiSe, YSi, CaSn, SrPb, and so on [27–34], exotic band crossings have been frequently reported. Since $YbBi_2$ shares similarity with the above-mentioned compounds in their crystal structures and symmetries, analogous properties, including small and open FS and nontrivial topological electronic states, could be expected therein. Note that in the title compound a $B^{1.6}$-dependent MR has been observed, while the actual mechanism to bring about such a situation is still an open question [22]. This therefore motivates us to study the correlation between its MR and electronic properties in this ever-overlooked compound.

In this paper, we have successfully synthesized high-quality $YbBi_2$ single crystals; measured their magnetization (M), specific heat (C_p), longitudinal resistivity (ρ_{xx}), Hall resistivity (ρ_{xy}); and calculated their electronic band structures. Our results suggest that this compound harbors nontrivial electronic properties with open FS sheets and balanced carrier densities, and the nonsaturating MR and its angular (φ) dependence are governed by the carrier compensation and FS anisotropy, respectively.

II. METHODS

A. Experimental details

High-quality single crystals of $YbBi_2$ were grown by a conventional flux method. Yb and Bi powders with the molar ratio of Yb : Bi = 3:7 were carefully mixed, placed into an alumina crucible, and then sealed in a quartz tube. The quartz tube was heated to 1073 K in 12 h, remained for 24 h, and was slowly cooled to 573 K in 500 h, at which the residual Bi flux was decanted using a centrifuge. As shown in the inset of Fig. 1(b), large platelike crystals with metallic luster were obtained.

X-ray diffraction (XRD) patterns were obtained with a Rigaku D/Max-2200/PC diffractometer using nickel filtered Cu $K\alpha$ radiation. Element composition and mapping were checked by a scanning electron microscope equipped with an energy-dispersive x-ray (EDX) spectrometer. X-ray photoelectron spectra (XPS) were examined by using a Thermo ESCALAB 250 system with an Al $K\alpha$ source ($h\nu = 1486.6$ eV). Magnetic properties were measured by a superconducting quantum interference device (SQUID) magnetometer. Specific heat (C_p) measurement was performed by thermal relaxation methods on a physical property measurement system (PPMS-9 T). Electrical transport was studied by using the standard four-probe method on a PPMS-14 T.

B. Theoretical details

Electronic structure calculations were carried out by the density functional theory employing a plane-wave basis projected augmented wave method as implemented in the Vienna *ab initio* simulation package [35,36]. Correlations between the nuclei and electrons were modeled by the generalized gradient approximation (GGA) of Perdew, Burke, and Ernzerhof

(PBE) exchange potential [37,38]. Energy cutoff of the plane-wave basis was set to 500 eV with a k mesh of $9 \times 9 \times 17$ for self-consistent calculations. The convergence criteria for energy and force were set to 1×10^{-6} eV and 0.01 eV/Å, respectively. In our calculation, 24 valence electrons and different Us were utilized to describe the Yb $4f$ states [39].

III. RESULT AND DISCUSSION

Figure 1(b) shows the XRD patterns of an $YbBi_2$ single crystal. Obviously, only a set of $(0k0)$ peaks is detected, suggesting that the exposed crystal surface is the ac plane. Note that the full width at half maximum (FWHM) of the (060) peak is approximately 0.15°, which implies that the as-grown crystals are of good quality. Here, the lattice parameter $b = 1.679$ nm can be extracted, in good agreement with the previous reports [22]. Figure 1(c) depicts the EDX spectra, where an approximate atomic ratio of Yb : Bi = 0.98 : 2.02 is determined. In addition, according to the element mapping presented in the inset of Fig. 1(c), one can see that Yb and Bi uniformly distribute across the sample surface, being suggestive of the absence of a Bi thin film or cluster therein. Figure 1(d) shows the Yb $4d$ core level spectra for $YbBi_2$. Clearly, our XPS spectra resemble those of $YbInCu_4$ (a mixed-valence system) [40], which evidences the presence of Yb^{2+} and Yb^{3+}. Note that XPS is a surface technique and hence may overestimate the amount of Yb^{3+} due to the apparent propensity of $YbBi_2$ in air to surface oxidation. Figure 1(e) and its inset plot the temperature (T) dependence of magnetic susceptibility (χ) for $B \| ac$ and $B \| b$ under 0.01 T, respectively. Small χ and its weak T dependence down to 75 K clearly indicate the predominance of nonmagnetic Yb^{2+} species with the electronic configuration $4f^{14}$ in $YbBi_2$. At low T, clear upturns are observed in χ, which could be associated with the Yb^{3+} impurities [41,42]. Figure 1(f) plots the variation of C_p as a function of T for this compound. As displayed, C_p monotonously increases from 2 to 300 K, where no anomalies concerning a phase transition could be tracked, suggesting the absence of long-range magnetic orderings therein [7]. The inset of Fig. 1(f) shows C_p/T as a function of T, from which determination of the Sommerfeld coefficient (γ) is allowed. An excellent fitting (red solid line) of the experimental data with the equation $C_p/T = \gamma + \beta T^2$ in the T range from 2 to 4 K yields $\gamma = 28.2\ \mathrm{mJ\ mol^{-1}\ K^{-2}}$. Note that this value is slightly larger than those of conventional materials ($\sim 1\ \mathrm{mJ\ mol^{-1}\ K^{-2}}$), like Cu [43], RPn series [5,7], etc., but is of the same order of magnitude as those observed in YbCdGe ($41\ \mathrm{mJ\ mol^{-1}\ K^{-2}}$) [41], YbCdSn ($28\ \mathrm{mJ\ mol^{-1}\ K^{-2}}$) [42], $YbFe_2Al_{10}$ ($35\ \mathrm{mJ\ mol^{-1}\ K^{-2}}$) [44], and so on. As reported, $\gamma \sim 28\ \mathrm{mJ\ mol^{-1}\ K^{-2}}$ remains a characteristic of ordinary metals [45]. Thus, heavy-fermion physics is not an issue here, and the f electron could not significantly contribute to the density of state. That is to say, the hybridization between f electrons and conduction ones in $YbBi_2$ is weak. Analogous cases have been observed in $YbTIn_5$ (T = Co, Rh, and Ir) [46,47], and $YbRh_2Ga$ [48].

Figure 2(a) shows ρ_{xx} of $YbBi_2$ as a function of T under different Bs. Here, T is plotted in a logarithmic scale to highlight the B effect on low-T transport properties. As shown, the zero-B ρ_{xx} continuously decreases from 217.7 $\mu\Omega$ cm at 300 K to 5.9 $\mu\Omega$ cm at 2 K, and thus the residual resistivity ratio $\mathrm{RRR} = \rho_{xx}(300\,\mathrm{K})/\rho_{xx}(2\,\mathrm{K}) \sim 36.9$, reflecting small defect scatterings in our samples. The inset of Fig. 2(a) depicts the zero-B ρ_{xx} below 30 K and its best fit with $\rho_{xx} = \rho_0 + aT^n$, where $\rho_0 = 5.83\ \mu\Omega$ cm, $a = 8.3 \times 10^{-4}\ \mu\Omega\,\mathrm{cm\,K^{-n}}$, and $n = 2.7$. Here, the obtained n is neither 2 for pure electron-electron scatterings [49] and phonon scatterings as observed in $YbSb_2$ [24] nor 5 for conventional electron-phonon scatterings [50], but almost close to those in LaBi (~2.99) [51], $MoAs_2$ (~3) [52], and $ZrSb_2$ (~3.16) [53], which implies that interband electron-phonon scatterings dominate the low-T transport in the title compound. With an application of B, ρ_{xx} at low T is significantly enhanced and consequently a definite upturn occurs above 2 T, where the metallic feature appears to be altered. Wang *et al.* propose that ρ_{xx} crossovers in semimetals can be simply understood by the conventional multiband approach instead of the B-induced excitonic-insulator transition which however, requires that the system is in close proximity to the quantum limit [45]. Therefore, we further check the T dependence of MR [inset of Fig. 2(b)] and normalized MR [Fig. 2(b)] under different Bs for $YbBi_2$. As shown, all the MR vs T curves exhibit metal-to-insulator-like transitions, whereas the normalized MR almost shares the same T dependences. It thus evidences that ρ_{xx} upturns in $YbBi_2$ could not be of B-induced gap origin [54], and hence the low-T phase is still metallic rather than insulating under B. Figure 2(c) shows the isothermal MR at various Ts, where I flows in the ac plane and B is applied along the b axis. As plotted, all MR increases with increasing B, without any sign of saturation. At 2 K, MR reaches 1.2×10^3% under 14 T, which is comparable to those of the RPtBi series [55], $MoGe_2$ [18], and so on. Figure 2(d) displays the B dependence of MR at 2 and 10 K and their best fits with an empirical power law $\mathrm{MR} = a'B^{n'}$. The same method has been employed to fit the ones at other Ts below 10 K. As shown in the inset of Fig. 2(d), a' shows weak T dependences and n' takes the values ~1.8. Similar cases have been observed in other compensated semimetals, such as $MoAs_2$ [10], YbAs [56], and so on, which is always ascribed to the slight imbalance between electron and hole concentrations. It follows that in $YbBi_2$ B-induced ρ_{xx} plateaus and metal-to-insulator-like transitions may be figured out by similar ways performed in these systems. To shed more light on the transport behaviors, we measure ρ_{xy} at different Ts. In Fig. 2(e), ρ_{xy} shows a nonlinear B dependence, which implies that the title compound is a multiband system [56]. Additionally, one can find that the slope of ρ_{xy} changes from negative to positive with the increase of T, implying that the transport property at low T is electronlike in contrast with the hole conduction at high T. To analyze the data, we employ a simple two-band model with one electron and one hole band as performed for several other multiband systems [56]:

$$\rho_{yx}(B) = \frac{B}{e}\frac{\left(n_h\mu_h{}^2 - n_e\mu_e{}^2\right) + (n_h - n_e)\mu_h{}^2\mu_e{}^2B^2}{(n_h\mu_h + n_e\mu_e)^2 + (n_h - n_e)^2\mu_h{}^2\mu_e{}^2B^2}.$$

An attempt to directly fit this two-band model to ρ_{yx} measured at 2 K [Fig. 2(f)] yields $n_h = 5.17 \times 10^{20}\ \mathrm{cm^{-3}}$, $n_e = 5.31 \times 10^{20}\ \mathrm{cm^{-3}}$, $\mu_h = 1525\ \mathrm{cm\ V^{-1}\ s^{-1}}$, and $\mu_e = 1549\ \mathrm{cm\ V^{-1}\ s^{-1}}$. One can see that in $YbBi_2$ n_h and n_e are not

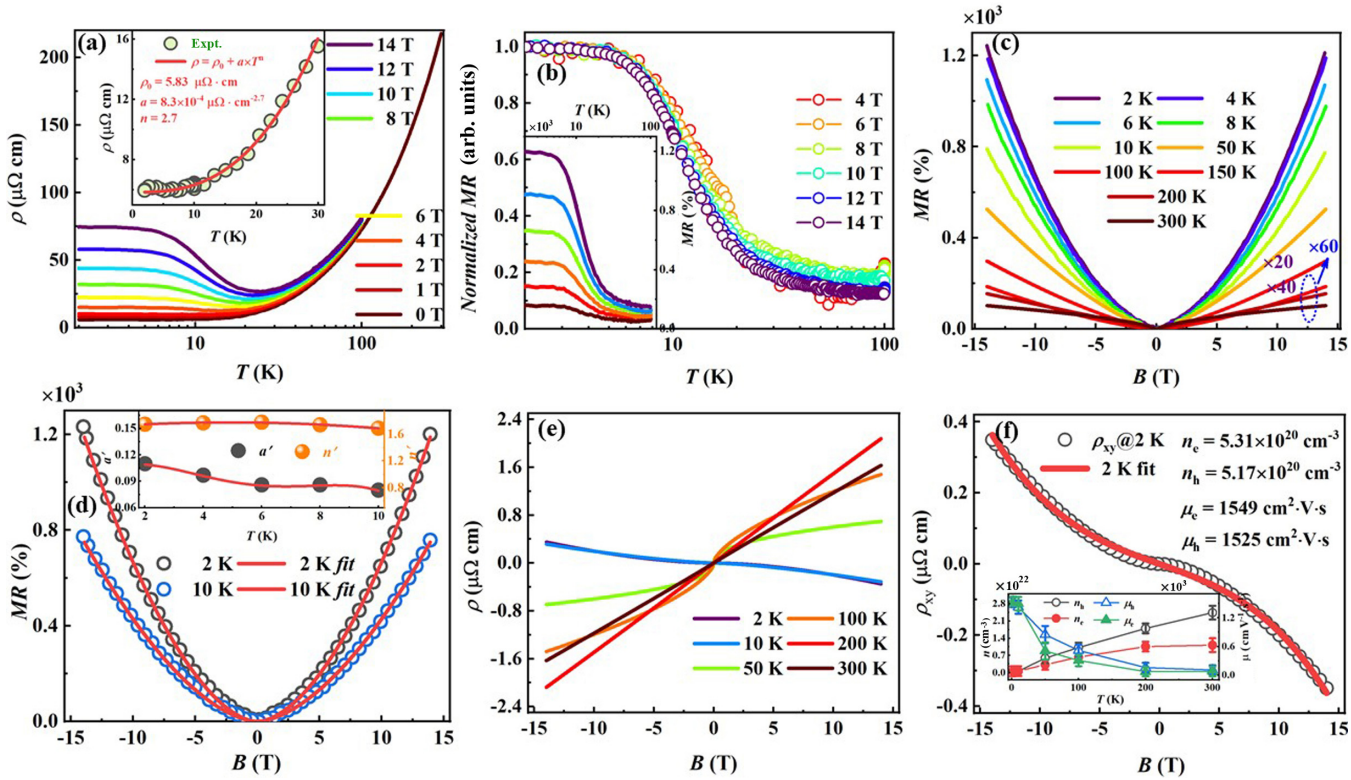

FIG. 2. (a) ρ_{xx} as a function of T under different Bs for $YbBi_2$. Inset plots the low-T ρ_{xx} under zero B and its fit to $\rho_{xx} = \rho_0 + aT^n$ ($\rho_0 = 5.83\,\mu\Omega\,\mathrm{cm}$, $a = 8.3 \times 10^{-4}\,\mu\Omega\,\mathrm{cm\,K^{-n}}$, and $n = 2.7$). (b) T-dependent normalized MR = MR(T)/MR(2 K) under various Bs. The inset shows the T dependence of MR for $YbBi_2$. (c) MR vs B at different Ts. (d) MR at 2 and 10 K, and their fits to MR $= a'B^{n'}$. Inset exhibits the variation of a' and n' as a function of T between 2 and 10 K. (e) B dependence of ρ_{xy} at different Ts. (f) ρ_{xy} as a function of B at 2 K and its fit to a two-band model. The inset shows the variation of n_h and n_e, and μ_h and μ_e as a function of T.

perfectly compensated, and $\mu_h(\mu_e)$ is one or two orders of magnitude less than those reported in *RPn* [5], NbP [4], and so on. Hence, it could be easily understood that $YbBi_2$'s MR shows a slight deviation from the perfect B^2 dependence and is smaller than that of *RPn* [5–7], $PtBi_2$ [8], and so on. The inset of Fig. 2(f) displays the T dependence of n_h and n_e, and μ_h and μ_e. As can be seen, with T increasing, n_h and n_e increase, while μ_h and μ_e decrease.

$YbBi_2$ crystallizes in a layered structure, and thus anisotropic electronic properties can be expected. Here, we carefully perform the φ-dependent MR measurements at 2 K to examine its FS anisotropy. Figure 3(a) depicts simple sketches of the experimental setup, where I flows in the *ac* plane, and B rotates in a plane normal to I [transverse configuration (TC)], and rotates from the b axis to I [transverse to longitudinal configuration (TLC)]. Here, φ is measured from the b axis. Figure 3(b) shows a polar plot of the φ-dependent MR under 2, 6, 10, and 14 T in the TC mode. It can be seen that all the MR(φ) curves have twofold symmetries. As φ increases, MR shows maxima for $B\|b$ and minima for $B\|ac$, implying that charge carriers move in minimal and maximal cyclotron orbits [57], respectively. Under 14 T, $\mathrm{MR_{max}} \sim 1200\%$ and $\mathrm{MR_{min}} \sim 326\%$, which yields an anisotropic ratio of MR [$\delta = \mathrm{MR_{max}/MR_{min}}$] ~368%. Generally, the symmetry of a projected FS profile onto the plane normal to I can be extracted from the polar plot of MR curves [57]. Thus, this system and hence its FSs have inversion and C_2 symmetries. Figure 3(c) shows the MR as a function of B at different φs. Obviously, MR increases with the increasing B at a fixed φ, but decreases with the increasing φ under the same B. This is consistent with the data shown in Fig. 3(b). Furthermore, we find that all the MR vs B curves in Fig. 3(c) can be collapsed onto a single one at 0° [Fig. 3(d)] with a scaling factor ε_φ [54]. The inset of Fig. 3(c) schematically shows the scaling approach with the MR data at 0° and 90°, and scaling orientation (the red arrow). A similar case has been observed in WTe_2 [54], graphite [58], high-T_c superconductors [59], etc., where the electronic properties are anisotropic and hence the φ-dependent quantity $Q(B, \varphi)$ commonly has the scaling behavior $Q(B, \varphi) = Q(\varepsilon_\varphi B)$ [54,58,59]. Here, $\varepsilon_\varphi B$ is the reduced B, and $\varepsilon_\varphi = (\cos^2\varphi + \gamma^{-2}\sin^2\varphi)^{1/2}$ reflects effective electron mass (m^*) anisotropy [54,58,59], with γ^2 being the ratio of m^* of electrons moving in the directions given by $\varphi =$ 0° and 90°. Note that in the semiclassical model, $\rho_{xx} = 1/ne\mu$ and $\mu = e\tau/m^*$ (τ is the relaxation time). It follows that m^* anisotropy plays a crucial part in the φ-dependent MR and thus FS anisotropy of materials. As for $YbBi_2$, its $\gamma \sim 1.7$ can be determined by fitting the φ-dependent ε_φ in the inset of Fig. 3(d), which is definitely much smaller than what one would naively expect for a two-dimensional (2D) system, such as graphite (12.1) [58], suggesting that the title compound is in fact electronically three dimensional (3D) with a small anisotropy. Figure 3(e) displays a polar plot of MR as a function of φ under 2, 6, 10, and 14 T in the TLC mode. One can clearly see that the anisotropic MR curves also have twofold symmetries. As expected, their maxima and minima appear at

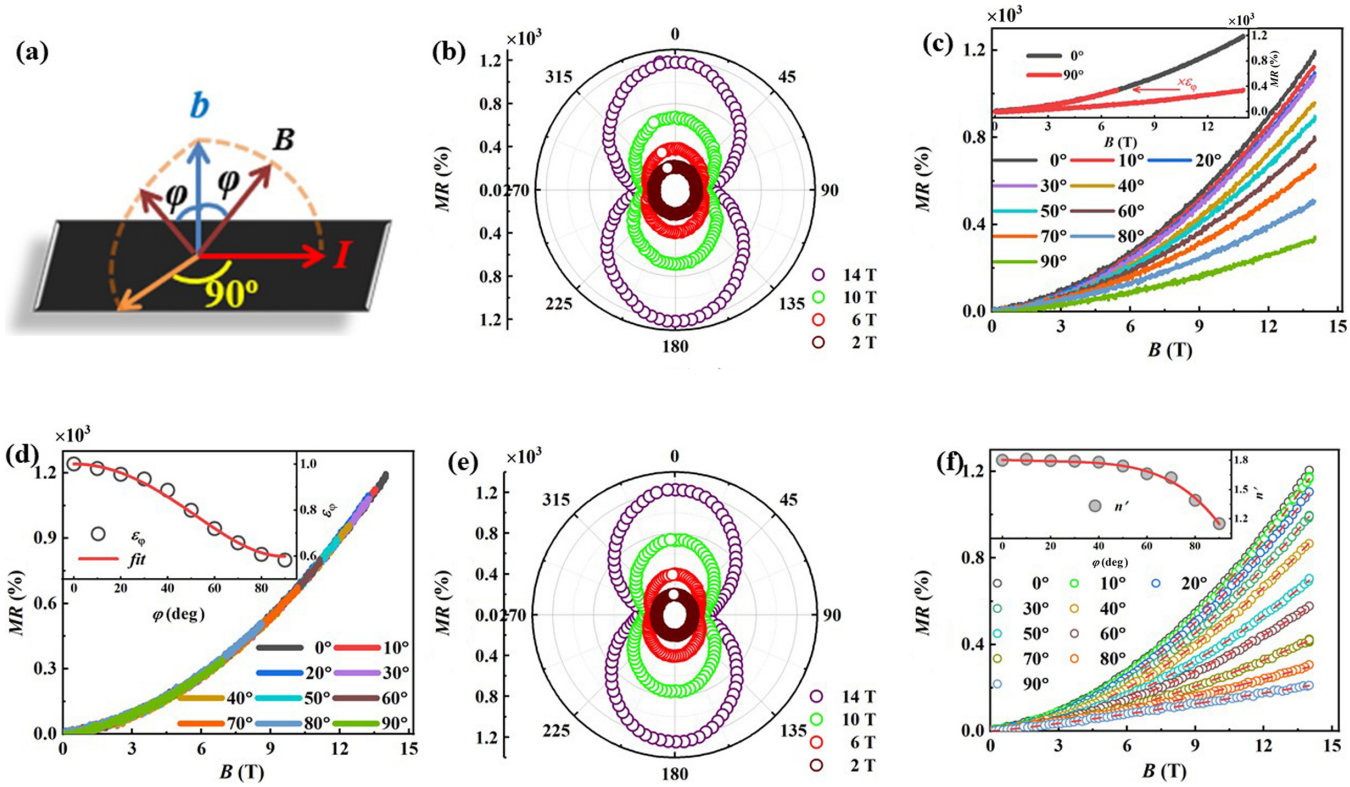

FIG. 3. (a) Experimental setups for the φ-dependent MR measurements in TC and TLC modes. (b) MR measured in TC mode as a function of φ under different Bs at 2 K. (c) Isothermal MR measured in TC mode at different φs. The inset shows a schematic for the scaling operation (the data at 90° and 2 K are used as an example). (d) Data in (c) replotted with B scaled by a factor ε_θ. The inset displays the φ dependence of ε_φ, and its fit to $\varepsilon_\varphi = (\cos^2\varphi + \gamma^{-2}\sin^2\varphi)^{1/2}$ with $\gamma \sim 1.7$. (e) MR measured in TLC mode as a function of φ under different Bs at 2 K. (f) MR measured in TLC mode as a function of B at different φs and 2 K. The inset shows the variation of n' as a function of φ at 2 K.

$\varphi = 0°$ and $\varphi = 90°$, respectively, because of the orbit origin. Here, the out of plane B component decreases with φ increasing, which further enlarges δ (~583%). Figure 3(f) shows the MR isotherms for different B orientations from $B \| b$ ($\varphi = 0°$) to $B \| I$ ($\varphi = 90°$). As seen, MR decreases with increasing φ at fixed B. We fit the B-dependent MR at different φs with MR $= a'B^{n'}$ and find that the obtained n' in the inset of Fig. 3(f) monotonously decreases from 1.8 ($\varphi = 0°$) to 1.2 ($\varphi = 90°$). That is, MR isotherms exhibit unsaturated behaviors all along in $YbBi_2$. Note that at $\varphi = 90°$ ($B \| I$) the pronounced B dependence of MR contradicts the expectation of a 2D system where only the normal B component ($|B\cos\varphi|$) contributes to MR; i.e., MR should be B independent in this case [54]. It follows that a 3D FS topology is more likely to determine the MR anisotropy in $YbBi_2$.

Figure 4(a) plots the M isotherms along the b axis at various Ts for $YbBi_2$. As seen, M oscillations emerge below 20 K, reflecting the high quality of our samples [7]. Note that isothermal M measurements have also been carried out for the $B \| ac$ plane (Fig. S1(a) in the Supplemental Material [60] (also see [61,62]), while no traceable M oscillations can be observed, suggesting the presence of 2D-like FS sheets in the title compound [63]. Figure 4(b) shows the oscillatory component of M (ΔM) after subtracting a smooth background. It can be found that the oscillatory pattern is the period in $1/B$, as expected from successive emptying of the Landau levels (LL) with increasing B. In the upper-right inset of Fig. 4(b), we exhibit the fast Fourier transformation (FFT) spectra of these M oscillations. One can find a single peak located at the frequency (F_α) ~ 38.3 T, which agrees with the results in Ref. [22]. The lower-right inset of Fig. 4(b) shows the normalized FFT amplitudes as a function of T. As seen, a rough fit of these experimental data to the thermal damping factor $R_T = (\lambda T)/\sinh(\lambda T)$ in the Lifshitz-Kosevich formula yields $m^* \sim 0.06m_e$. Here, $\lambda = 2\pi^2 k_B m^*/(e\hbar\bar{B}) = 14.69m^*/B$ [2], and the average B ($\bar{B}$) is set as 4.1 T [$1/B = (1/B_{start} + 1/B_{end})/2$] with $B_{start} = 2.9$ T and $B_{end} = 7$ T. According to the Onsager relation $F = (\Phi_0/2\pi^2)A_F$ [2], the cross-sectional area of FS (A_F) normal to B is calculated to be 3.7×10^{-3} Å^{-2}. By assuming a circular cross section [2], a very small Fermi momentum $k_F \sim 0.034$ Å^{-1} is determined. Thus, one can obtain the Fermi velocity $v_F = \hbar k_F/m^* \sim 2.1 \times 10^6$ m/s, and Fermi energy $E_F = m^* v_F^2 \sim 0.13$ eV. The upper-left inset of Fig. 4(c) exhibits the Dingle plot for F_α, from which the Dingle T (T_D) is estimated to be ~2.2 K. Correspondingly, the quantum lifetime $\tau_Q^\alpha = \hbar/2\pi k_B T_D \sim 7.7 \times 10^{-14}$ s and quantum mobility $\mu_q \sim 225$ cm V^{-1} s^{-1}. Figure 4(c) plots the LL fan diagram for the F_α band, where ΔM peaks and valleys are assigned as N-3/4 and N-1/4 (LL indices), respectively [64,65], and fall onto a straight line. A linear fitting of N vs $1/B$ gives an intercept of 0.44 and thus the Berry phase $\phi_B = 2\pi(0.44 + \delta)$ [66]. Here, δ is the FS dimension-dependent correction to a phase shift, of which the value varies from 0 for 2D FS to +1/8 or –1/8 for a minimum or maximum cross section of 3D FS, respectively [6]. Next, we check the dimension of the F_α band before evaluating the value of ϕ_B. Figure S1 in

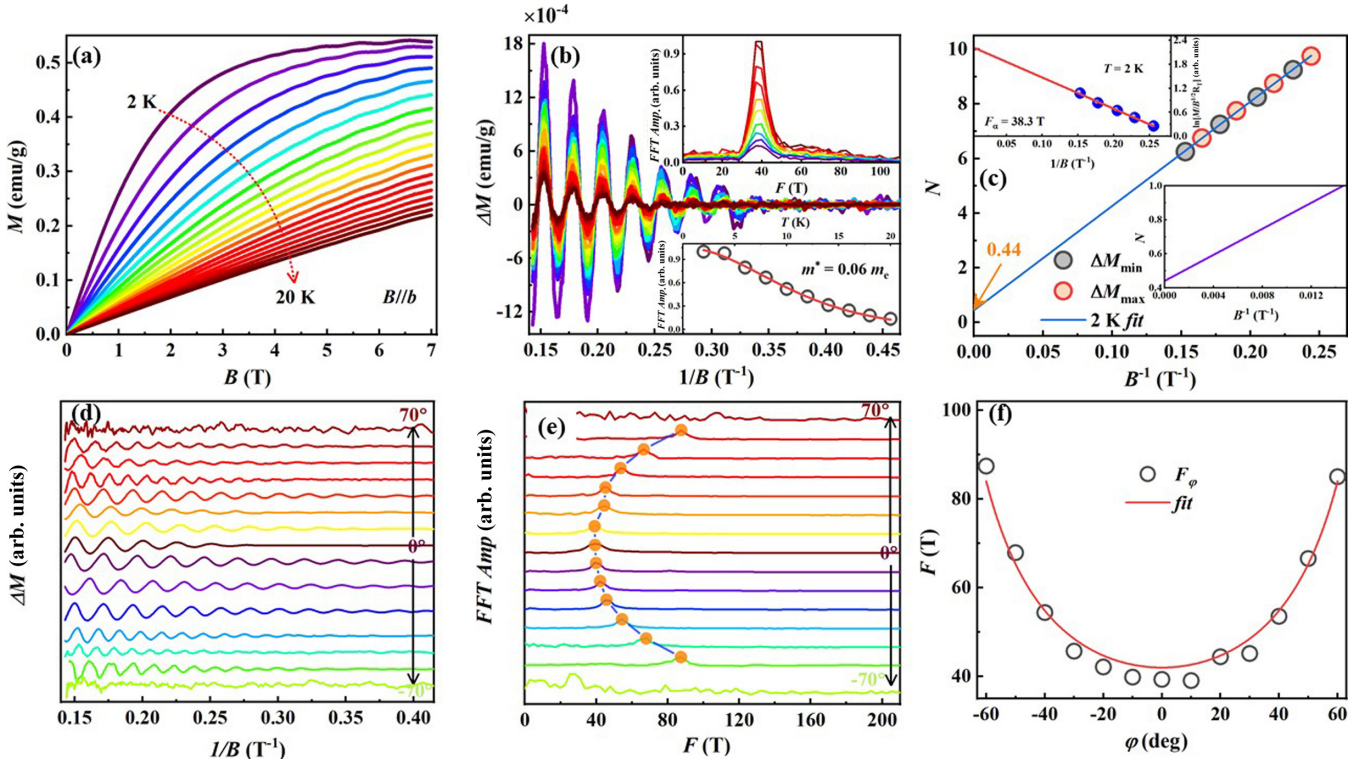

FIG. 4. (a) M isotherms for $B\|b$ axis at different Ts. (b) ΔM vs $1/B$ at different Ts. The upper inset shows the FFT spectra of ΔM at different Ts. The lower inset displays the T dependence of normalized FFT amplitudes and its fit (red line) to R_T in the Lifshitz-Kosevich formula. (c) LL index fan diagram for F_α. The lower-right inset enlarges the intersection. The upper-left inset shows the Dingle plot for F_α at 2 K. (d) ΔM vs $1/B$ at different φs. (e) The FFT spectra of ΔM at different φs. (f) φ-dependent F at 2 K. The red solid line is the result of fitting $F(\varphi) = F_0/[\cos^2(\varphi) + \varepsilon^2\sin^2(\varphi)]^{1/2}$ to experimental data.

the Supplemental Material [60] displays the M isotherms at different φs and 2 K. Here, φ is also measured from the b axis and B is rotated from the b axis to ac plane. As seen, M oscillations only occur in the narrow φ range between –60° and 60°. Figure 4(d) presents the ΔM against $1/B$ at different φs after background subtraction, where the oscillation pattern displays a clear evolution with the increasing φ. Here, we plot the ΔM vs $1/B$ curves in the φ range from –70° to 70°. Figure 4(e) shows their FFT spectra, where only one F can be observed at all the φs. Figure 4(f) depicts the φ dependence of F_α, where $F_\alpha(\varphi) = F_\alpha(-\varphi)$ and $F_\alpha(\varphi)$ takes a minimum at 0°. To gain more information on the FS sheet associated with the F_α band, we further fit the φ-dependent F_α with $F(\varphi) = F_0/[\cos^2(\varphi) + \varepsilon^2\sin^2(\varphi)]^{1/2}$ [6], where $F(\varphi)$ denotes the F at a certain φ, and F_0 is the F at 0°. Here, FS has a 3D sphere [$F(\varphi) = F_0$] and a 2D cylinder [$F(\varphi) = F_0/\cos\varphi$] shape for $\varepsilon = 1$ and 0, respectively [65]. Evidently, the experimental data in the inset of Fig. 4(f) can be well reproduced by this ellipsoid function with $\varepsilon \sim 0$, suggesting that the F_α branch harbors a small cylindrical FS topography. Therefore, $\phi_B = 2\pi(0.44 + \delta) = 0.88\pi$ for the F_α band. Note that $\phi_B \sim \pi$ cannot be viewed as a smoking gun of topologically nontrivial materials [67–69]. It is a longstanding issue once the LL fan diagram is employed to extract ϕ_B. As performed in the literature, we fit the Lifshitz-Kosevich formula to the experimental data and find $\phi_B \sim 1.08\pi$ (Fig. S2 in the Supplemental Material [60]). Although the preceding analysis seemingly supports the presence of a nontrivial ϕ_B in $YbBi_2$, it still should be pointed out that this phase factor could be complicated by other contributions, such as Maslov correction, dynamic phase factor, and so on [67–69]. Incidentally, Ohara *et al.* performed the M isotherm measurements for $YbBi_2$ by using a field-modulation technique in fields up to 8.5 T and observed more than one F in the FFT spectra [22]. To reveal other Fs, we measured the M isotherms up to 14 T (Fig. S3 in the Supplemental Material [60]). Unfortunately, still only a single $F \sim 38.3$ T occurs in the FFT spectra. Note that in Ref. [26] Sato *et al.* find that more Fs could be detected in the field-modulation method rather than the static method. Therefore, only a single F observed in our measurements is entirely possible. It is possible that larger fields ($B > 14$ T) or other techniques can be adopted to reveal more Fs, which are not available to us at this moment. Except for F (~38.3 T), other physical properties extracted from the quantum oscillations measured at 7 and 14 T are nearly the same.

In support for these findings, the DFT calculations are performed for $YbBi_2$. Figure 5(a) shows the calculated bulk band structures with spin-orbit couplings along the high-symmetry lines. Clearly, various bands cross the Fermi level, which is consistent with the metallic feature of this compound. More importantly, several band crossings emerge along the high-symmetry lines such as a fourfold degenerate Dirac nodal line along the high-symmetry T-Z, fourfold degenerate Dirac points along the high-symmetry Z point, and so on. Orbital-resolved electronic band structures show that the band crossings are composed of Bi p orbitals. Note that the

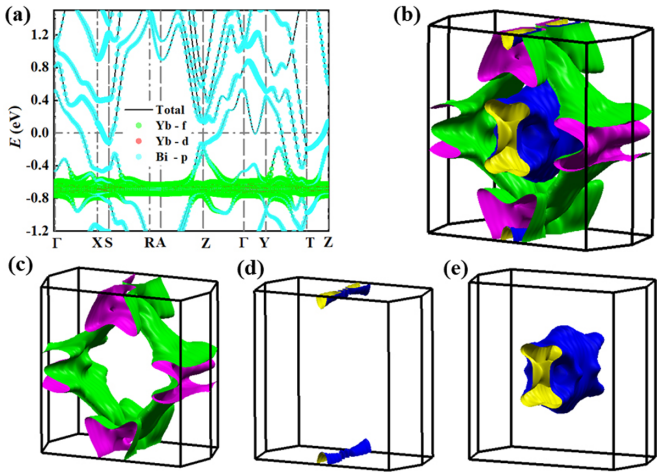

FIG. 5. (a) Band structures and (b) FS of $YbBi_2$, respectively. (c) An electron FS sheet; (d) a cylindrical electron FS sheet; (e) a hole FS sheet.

degeneracy of the Dirac line node could not be lifted in the presence of SOC due to the protection by nonsymmorphic glide mirror symmetry. A similar case has been observed in ZrSiS [70]. Thus, $YbBi_2$ could be a topological nodal-line semimetal candidate. Figure 5(b) plots its bulk FS, from which two electron sheets and a hole sheet are revealed. The three FS sheets are plotted separately in Figs. 5(c)–5(e). As shown, one electron FS sheet [Fig. 5(c)] locates around the BZ boundary, and the other electron FS sheet with $k_F \sim 0.028$ Å^{-1} [Fig. 5(d)] distributes along the T-Z direction (b directions in the conventional cell). Note that this k_F is comparable to the experimental results. Hence, those de Haas–van Alphen (dHvA) oscillations could be associated with the FS sheet shown in Fig. 5(d). In addition, one can find that as presented in Fig. 5(e) a hole sheet hosts a nearly cylindrical FS along the (110) directions (b lattice vector in conventional cell) centered at the Γ point. It thus can be seen that the FS of $YbBi_2$ is highly anisotropic and elongates along the b axis. Note that $U = 4$ eV is utilized to describe the Yb $4f$ states herein. Additionally, as shown in Fig. S4 of the Supplemental Material [60], the band structures with $U = 0$, 2, and 6 eV have been calculated and discussed.

Next, we attempt to unveil the underlying physics behind the large and anisotropic MR in $YbBi_2$. Hereinbefore, the presence of a nontrivial ϕ_B has been confirmed in this compound, suggesting that it is a potential topological material. Hence, contributions from the B lifting of topologically protected backscattering to MR should be checked. For $YbBi_2$, its $\mu_h(\mu_e)/\mu_q \sim 7$, which is much smaller than those obtained in the topological semimetals, like Cd_3As_2 ($\sim 10^4$) [9] and NbAs ($\sim 10^3$) [71], implying that small angle scatterings are dominant in the transport and thus its MR could not be of topological protection origin. In Figs. 4(f) and 5(d), one may notice that in $YbBi_2$ there exist several sheets with open FSs lying inside the layer plane. A similar case has been observed in $PdCoO_2$ [72], $MoAs_2$ [10], ZrSiS [19], SiP_2 [15], γ-$PtBi_2$ [14], and so on, where large MR emerges as well. It should be emphasized that in these systems their MR shows parabolic B dependences only when I flows along the axes of open FS sheets and B is applied in an orthogonal direction; i.e., $I \perp B$ [57]. In our measurements, I flows in the ac plane and is vertical to B ($B \| b$), whereas the open FSs elongate along the b axis. More importantly, as shown in Fig. 3(f), the B-dependent MR presents unsaturated behaviors at different φs, which is contradictory to the cases governed by open orbits; i.e., the MR should be saturated at certain φs [57]. Thus, open FSs also do not work for the large MR in $YbBi_2$. Except for this B lifting of topological protection and open orbits, carrier compensation usually severs as a viable cause for MR with an almost parabolic B dependence in many semimetals [5,7,18,49]. Recently, Zhao *et al.* found that MoAlB [73], which is an isostructural analog of $YbBi_2$ and harbors open FSs along the b axis, shows a paraboliclike MR. Note that in their MR measurements B is applied along the b axis and I flows in the ac plane as well. After checking its FS topology, they contribute the unsaturated MR in MoAlB to compensated carrier concentrations [73]. Since $YbBi_2$ and MoAlB share similarity in crystal and electronic structures, their large MR could be of the same origin, i.e., the equisized electron and hole densities. Indeed, as extracted from the ρ_{xy} data, $n_h \sim n_e$, which may be a possible cause of the paraboliclike MR in $YbBi_2$. In addition, this compound harbors anisotropic FS topology that could have an effect on its φ-dependent MR. For $B \| b$, the charge carriers with cyclotron motion are locked around the FSs normal to the b axis. As referred above, the perpendicular cross-section area of FS is the smallest in this case, and thus a large MR occurs. Once B is rotated from the b axis to the ac plane, the perpendicular cross-section area of the FS changes and becomes infinite for $B \| ac$. Correspondingly, the cyclotron orbits of charge carriers increase and meanwhile the MR monotonously drops, which agrees well with the anisotropic MR shown in Fig. 3(b). It thus can be seen that in $YbBi_2$ the φ-dependent MR is associated with its FS anisotropy.

IV. CONCLUSION

We have succeeded in growing high-quality $YbBi_2$ single crystals and carrying out their M, MR, and ρ_{xy} measurements; electronic band structure calculations, etc. Nonzero ϕ_B extracted from the M oscillations suggests that the title compound harbors nontrivial electronic properties. φ-dependent M oscillations reveal the presence of open FSs in this compound. Its angular MR with significant φ dependences implies that the FS is highly anisotropic. An analysis of ρ_{xy} data manifests that multiple charge carriers with almost equisized densities participate in transport. All these findings are consistent with the theoretical results. After checking several possible mechanisms, we have found that the giant and φ-dependent MR in $YbBi_2$ could be closely associated with the nearly compensated carrier densities and FS anisotropy, respectively. Our work proves that the title compound concurrently shows nontrivial topological electronic states, open FSs, and compensated carrier concentrations, and provides an ideal material platform to study different MR mechanisms.

ACKNOWLEDGMENTS

This work was supported by the National Natural Science Foundation of China (Grants No. 12174039 and No. 62005027), Key University Science Research Project of

Jiangsu Province (Grant No. 19KJA530003), Natural Science Foundation of Jiangsu Province (Grant No. BK20200345), Open Fund of Fujian Provincial Key Laboratory of Quantum Manipulation and New Energy Materials (Grant No. QMNEM1903), and the Big Data Computing Center of Southeast University.

[1] M. N. Ali, J. Xiong, S. Flynn, J. Tao, Q. D. Gibson, L. M. Schoop, T. Liang, N. Haldolaarachchige, M. Hirschberger, N. P. Ong, and R. J. Cava, Nature (London) **514**, 205 (2014).
[2] L. P. He, X. C. Hong, J. K. Dong, J. Pan, Z. Zhang, J. Zhang, and S. Y. Li, Phys. Rev. Lett. **113**, 246402 (2014).
[3] X. Huang, L. Zhao, Y. Long, P. Wang, D. Chen, Z. Yang, H. Liang, M. Xue, H. Weng, Z. Fang, X. Dai, and G. Chen, Phys. Rev. X **5**, 031023 (2015).
[4] C. Shekhar, A. K. Nayak, Y. Sun, M. Schmidt, M. Nicklas, I. Leermakers, U. Zeitler, Y. Skourski, J. Wosnitza, Z. Liu, Y. Chen, W. Schnelle, H. Borrmann, Y. Grin, C. Felser, and B. Yan, Nat. Phys. **11**, 645 (2015).
[5] L.-Y. Fan, F. Tang, W. Z. Meng, W. Zhao, L. Zhang, Z. D. Han, B. Qian, X.-F. Jiang, X. M. Zhang, and Y. Fang, Phys. Rev. B **102**, 104417 (2020).
[6] Y. Fang, F. Tang, Y. R. Ruan, J. M. Zhang, H. Zhang, H. Gu, W. Y. Zhao, Z. D. Han, W. Tian, B. Qian, X. F. Jiang, X. M. Zhang, and X. Ke, Phys. Rev. B **101**, 094424 (2020).
[7] H. Gu, F. Tang, Y.-R. Ruan, J.-M. Zhang, R.-J. Tang, W. Zhao, R. Zhao, L. Zhang, Z.-D. Han, B. Qian, X.-F. Jiang, and Y. Fang, Phys. Rev. Materials **4**, 124204 (2020).
[8] W. Gao, N. Hao, F.-W. Zheng, W. Ning, M. Wu, X. Zhu, G. Zheng, J. Zhang, J. Lu, H. Zhang, C. Xi, J. Yang, H. Du, P. Zhang, Y. Zhang, and M. Tian, Phys. Rev. Lett. **118**, 256601 (2017).
[9] T. Liang, Q. Gibson, M. N. Ali, M. Liu, R. J. Cava, and N. P. Ong, Nat. Mater. **14**, 280 (2015).
[10] R. Lou, Y. F. Xu, L.-X. Zhao, Z.-Q. Han, P.-J. Guo, M. Li, J.-C. Wang, B.-B. Fu, Z.-H. Liu, Y.-B. Huang, P. Richard, T. Qian, K. Liu, G.-F. Chen, H. M. Weng, H. Ding, and S.-C. Wang, Phys. Rev. B **96**, 241106(R) (2017).
[11] K. Wang, D. Graf, L. Li, L. Wang, and C. Petrovic, Sci. Rep. **4**, 7328 (2014).
[12] Y. Li, L. Li, J. Wang, T. Wang, X. Xu, C. Xi, C. Cao, and J. Dai, Phys. Rev. B **94**, 121115(R) (2016).
[13] J. Hu, J. Y. Liu, D. Graf, S. M. A. Radmanesh, D. J. Adams, A. Chuang, Y. Wang, I. Chiorescu, J. Wei, L. Spinu, and Z. Q. Mao, Sci. Rep. **6**, 18674 (2016).
[14] B. Wu, V. Barrena, H. Suderow, and I. Guillamón, Phys. Rev. Research **2**, 022042(R) (2020).
[15] Y. Zhou, Z. Lou, S. N. Zhang, H. Chen, Q. Chen, B. Xu, J. Du, J. Yang, H. Wang, C. Xi, L. Pi, Q. S. Wu, O. V. Yazyev, and M. Fang, Phys. Rev. B **102**, 115145 (2020).
[16] Z. Wang, M. Huang, J. Zhao, C. Chen, H. Huang, X. Wang, P. Liu, J. Wang, J. Xiang, C. Feng, Z. Zhang, X. Cui, Y. Lu, S. A. Yang, and B. Xiang, Phys. Rev. Materials **4**, 041001(R) (2020).
[17] F. F. Tafti, Q. D. Gibson, S. K. Kushwaha, N. Haldolaarachchige, and R. J. Cava, Nat. Phys. **12**, 272 (2016).
[18] Y.-F. Huang, W.-L. Zhu, Y.-Y. Wang, Q.-X. Dong, L.-B. Zhang, C.-S. Li, H. OuYang, Z.-A. Ren, and G.-F. Chen, Phys. Rev. B **103**, 134116 (2021).
[19] Y.-Y. Lv, B.-B. Zhang, X. Li, S.-H. Yao, Y. B. Chen, J. Zhou, S.-T. Zhang, M.-H. Lu, and Y.-F. Chen, Appl. Phys. Lett. **108**, 244101 (2016).
[20] N. Kumar, Y. Sun, N. Xu, K. Manna, M. Yao, V. Süss, I. Leermakers, O. Young, T. Förster, M. Schmidt, H. Borrmann, B. Yan, U. Zeitler, M. Shi, C. Felser, and C. Shekhar, Nat. Commun. **8**, 1642 (2017).
[21] Q. Chen, Z. Lou, S. N. Zhang, Y. Zhou, B. Xu, H. Chen, S. Chen, J. Du, H. Wang, J. Yang, Q. S. Wu, O. V. Yazyev, and M. Fang, Phys. Rev. B **104**, 115104 (2021).
[22] S. Ohara, G. F. Chen, I. Oguro, and I. Sakamoto, Physica B **281-282**, 752 (2000).
[23] S. Gołąb and B. Wiendlocha, Phys. Rev. B **99**, 104520 (2019).
[24] L. L. Zhao, S. Lausberg, H. Kim, M. A. Tanatar, M. Brando, R. Prozorov, and E. Morosan, Phys. Rev. B **85**, 214526 (2012).
[25] M. J. Winiarski, B. Wiendlocha, S. S. Gołąb, S. K. Kushwaha, P. P. Wiśniewski, D. Kaczorowski, J. D. Thompson, R. J. Cava, and T. Klimczuk, Phys. Chem. Chem. Phys. **18**, 21737 (2016).
[26] N. Sato, T. Kinokiri, T. Komatsubara, and H. Harima, Phys. Rev. B **59**, 4714 (1999).
[27] F. Tang, Y. Ren, P. Wang, R. Zhong, J. Schneeloch, S. A. Yang, K. Yang, P. A. Lee, G. Gu, Z. Qiao, and L. Zhang, Nature (London) **569**, 537 (2019).
[28] Z. Zhu, T.-R. Chang, C.-Y. Huang, H. Pan, X.-A. Nie, X.-Z. Wang, Z.-T. Jin, S.-Y. Xu, S.-M. Huang, D.-D. Guan, S. Wang, Y.-Y. Li, C. Liu, D. Qian, W. Ku, F. Song, H. Lin, H. Zheng, and J.-F. Jia, Nat. Commun. **9**, 4153 (2018).
[29] V. Saini, S. Sasmal, R. Kulkarni, B. Singh, and A. Thamizhavel, Phys. Rev. B **103**, 195154 (2021).
[30] L. X. Xu, Y. Y. Y. Xia, S. Liu, Y. W. Li, L. Y. Wei, H. Y. Wang, C. W. Wang, H. F. Yang, A. J. Liang, K. Huang, T. Deng, W. Xia, X. Zhang, H. J. Zheng, Y. J. Chen, L. X. Yang, M. X. Wang, Y. F. Guo, G. Li, Z. K. Liu, and Y. L. Chen, Phys. Rev. B **103**, L201109 (2021).
[31] W. Fan, S. Nie, C. Wang, B. Fu, C. Yi, S. Gao, Z. Rao, D. Yan, J. Ma, M. Shi, Y. Huang, Y. Shi, Z. Wang, T. Qian, and H. Ding, Nat. Commun. **12**, 2052 (2021).
[32] T. Zhang, Y. Jiang, Z. Song, H. Huang, Y. He, Z. Fang, H. Weng, and C. Fang, Nature (London) **566**, 475 (2019).
[33] F. Tang, H. C. Po, A. Vishwanath, and X. Wan, Nature (London) **566**, 486 (2019).
[34] M. G. Vergniory, L. Elcoro, C. Felser, B. A. Bernevig, and Z. Wang, Nature (London) **566**, 480 (2019).
[35] G. Kresse and J. Hafner, Phys. Rev. B **49**, 14251 (1994).
[36] G. Kresse and J. Furthmüller, Phys. Rev. B **54**, 11169 (1996).
[37] P. E. Blöchl, Phys. Rev. B **50**, 17953 (1994).
[38] J. P. Perdew, K. Burke, and M. Ernzerhof, Phys. Rev. Lett. **77**, 3865 (1996).
[39] S. L. Dudarev, G. A. Botton, S. Y. Savrasov, C. J. Humphreys, and A. P. Sutton, Phys. Rev. B **57**, 1505 (1998).
[40] S. Schmidt, S. Hüfner, F. Reinert, and W. Assmus, Phys. Rev. B **71**, 195110 (2005).

[41] A. Laha, S. Malick, R. Singha, P. Mandal, P. Rambabu, V. Kanchana, and Z. Hossain, Phys. Rev. B **99**, 241102(R) (2019).

[42] A. Laha, P. Rambabu, V. Kanchana, L. Petit, Z. Szotek, and Z. Hossain, Phys. Rev. B **102**, 235135 (2020).

[43] D. L. Martin, Phys. Rev. B **8**, 5357 (1973).

[44] J. L. Lv, R. Y. Chen, H. P. Wang, J. L. Luo, and N. L. Wang, Phys. Rev. B **95**, 235132 (2017).

[45] D. A. Gajewski, N. R. Dilley, E. D. Bauer, E. J. Freeman, R. Chau, M. B. Maple, D. Mandrus, B. C. Sales, and A. H. Lacerda, J. Phys.: Condens. Matter **10**, 6973 (1998).

[46] A. Polyakov, O. Ignatchik, B. Bergk, K. Götze, A. D. Bianchi, S. Blackburn, B. Prévost, G. Seyfarth, M. Côté, D. Hurt, C. Capan, Z. Fisk, R. G. Goodrich, I. Sheikin, M. Richter, and J. Wosnitza, Phys. Rev. B **85**, 245119 (2012).

[47] J. Sakaguchi, H. Tsutsumi, Y. Hirose, Y. Miura, F. Honda, H. Harima, R. Settai, and Y. Ōnuki, J. Phys. Soc. Jpn. **81**, SB059 (2012).

[48] G. F. Chen, I. Sakamoto, S. Ohara, T. Takami, H. Ikuta, and U. Mizutani, Phys. Rev. B **69**, 054435 (2004).

[49] Y. L. Wang, L. R. Thoutam, Z. L. Xiao, J. Hu, S. Das, Z. Q. Mao, J. Wei, R. Divan, A. Luican-Mayer, G. W. Crabtree, and W. K. Kwok, Phys. Rev. B **92**, 180402(R) (2015).

[50] J. Ziman, *Electrons and Phonons* (Oxford University Press, Oxford, 1960), Vol. 14.

[51] S. Sun, Q. Wang, P. -J. Guo, K. Liu, and H. Lei, New J. Phys. **18**, 082002 (2016).

[52] R. Singha, A. Pariari, G. K. Gupta, T. Das, and P. Mandal, Phys. Rev. B **97**, 155120 (2018).

[53] L.-L. Sun, Y.-Y. Wang, S. Xu, and T.-L. Xia, EPL **120**, 37002 (2017).

[54] L. R. Thoutam, Y. L. Wang, Z. L. Xiao, S. Das, A. Luican-Mayer, R. Divan, G. W. Crabtree, and W. K. Kwok, Phys. Rev. Lett. **115**, 046602 (2015).

[55] J. Chen, H. Li, B. Ding, E. Liu, Y. Yao, G. Wu, and W. Wang, Appl. Phys. Lett. **116**, 222403 (2020).

[56] W. Xie, Y. Wu, F. Du, A. Wang, H. Su, Y. Chen, Z. Y. Nie, S.-K. Mo, M. Smidman, C. Cao, Y. Liu, T. Takabatake, and H. Q. Yuan, Phys. Rev. B **101**, 085132 (2020).

[57] S. Zhang, Q. Wu, Y. Liu, and O. V. Yazyev, Phys. Rev. B **99**, 035142 (2019).

[58] D. E. Soule, Phys. Rev. **112**, 698 (1958).

[59] T. Ishida, K. Okuda, H. Asaoka, Y. Kazumata, K. Noda, and H. Takei, Phys. Rev. B **56**, 11897 (1997).

[60] See Supplemental Material at http://link.aps.org/supplemental/10.1103/PhysRevB.105.195114 for M isotherms up to 7 T at different φs and 2 K; dHvA oscillations at 2 K, and their fit to the LK formula; M isotherms up to 14 T at different Ts for $B\|b$; M isotherms up to 14 T at different φs and 2 K; FFT spectra at different φs and 2 K; φ-dependent F at 2 K and their fit to $F(\varphi) = F_0/[\cos^2(\varphi) + \varepsilon^2\sin^2(\varphi)]^{1/2}$; electronic band structures with different Us; also see Refs. [61,62].

[61] S. J. Lee, S. Y. Hong, I. R. Fisher, P. C. Canfield, B. N. Harmon, and D. W. Lynch, Phys. Rev. B **61**, 10076 (2000).

[62] M. Falkowski and A. M. Strydom, J. Phys.: Condens. Matter **27**, 395601 (2015).

[63] K.-W. Chen, S. Das, D. Rhodes, S. Memaran, T. Besara, T. Siegrist, E. Manousakis, L. Balicas, and R. E. Baumbach, J. Phys.: Condens. Matter **28**, 14LT01 (2016).

[64] J. B. He, Y. Fu, L. X. Zhao, H. Liang, D. Chen, Y. M. Leng, X. M. Wang, J. Li, S. Zhang, M. Q. Xue, C. H. Li, P. Zhang, Z. A. Ren, and G. F. Chen, Phys. Rev. B **95**, 045128 (2017).

[65] Y. J. Wang, D. D. Liang, M. Ge, J. Yang, J. X. Gong, L. Luo, L. Pi, W. K. Zhu, C. J. Zhang, and Y. H. Zhang, J. Phys.: Condens. Matter **30**, 155701 (2018).

[66] J. Hu, Z. Tang, J. Liu, Y. Zhu, J. Wei, and Z. Mao, Phys. Rev. B **96**, 045127 (2017).

[67] A. Alexandradinata, C. Wang, W. Duan, and L. Glazman, Phys. Rev. X **8**, 011027 (2018).

[68] A. Alexandradinata and L. Glazman, Phys. Rev. B **97**, 144422 (2018).

[69] C. Schindler, D. Gorbunov, S. Zherlitsyn, S. Galeski, M. Schmidt, J. Wosnitza, and J. Gooth, Phys. Rev. B **102**, 165156 (2020).

[70] S. Pezzini, M. R. van Delft, L. M. Schoop, B. V. Lotsch, A. Carrington, M. I. Katsnelson, N. E. Hussey, and S. Wiedmann, Nat. Phys. **14**, 178 (2018).

[71] Y. Luo, N. J. Ghimire, M. Wartenbe, H. Choi, M. Neupane, R. D. McDonald, E. D. Bauer, J. Zhu, J. D. Thompson, and F. Ronning, Phys. Rev. B **92**, 205134 (2015).

[72] H. Takatsu, J. J. Ishikawa, S. Yonezawa, H. Yoshino, T. Shishidou, T. Oguchi, K. Murata, and Y. Maeno, Phys. Rev. Lett. **111**, 056601 (2013).

[73] L. Zhao, L. Xu, L. Ding, H. Zuo, and Z. Zhu, Phys. Rev. B **102**, 075139 (2020).